Stepped and Swept Control-Based Continuation using Adaptive Filtering

Gaëtan Abeloos*,[1] Ludovic Renson[2] Christophe Collette[1] Gaëtan Kerschen[1]

April 2021

Abstract

This paper introduces a new online method for performing control-based continuation (CBC), speeding up the model-less identification of stable and unstable periodic orbits of nonlinear mechanical systems. The main building block of the algorithm is adaptive filtering which can ensure the non-invasiveness of the controller without the need for offline corrective iterations. Two different strategies, termed stepped and swept CBC, are then developed for performing the continuation steps. A beam featuring different artificial stiffness and damping nonlinearities is considered for the experimental demonstration of the proposed developments. The performance of the CBC strategies are compared in terms of running time and identification accuracy.

Keywords: Control-Based Continuation; Adaptive Filtering; Feedback Stabilization; Invasiveness Cancellation

1 Introduction

Time-invariant nonlinear systems are known to exhibit rich and complex behaviors with multiple branches of orbits — possibly unstable — interconnected by bifurcations and chaos. The characterization of such systems is most often performed theoretically using numerical continuation techniques which are quite sophisticated and advanced, see e.g. [1, 2, 3]. For nonlinear mechanical systems which vibrate when subjected to an external force, numerical continuation has been used for computing the steady-state behavior in response to harmonic forcing through frequency response curves (FRCs), the nonlinear counterpart of the frequency response functions of linear systems [4].

The experimental identification of FRCs of nonlinear mechanical systems is a much more challenging endeavor. Considering the harmonically-forced Duffing oscillator

$$\ddot{x}(t) + \dot{x}(t) + x(t) + x^3(t) = p \sin \omega t. \qquad (1)$$

as an illustrative example, several FRCs corresponding to increasing forcing amplitudes p are shown in Fig. 1. For ease of notation, the maximum displacement amplitude during the periodic oscillation is noted x. Because the superposition principle does no longer hold for nonlinear systems, the topology of FRCs changes with the forcing amplitude (e.g. the unstable branch absent from the blue FRC but present in the red FRC in Fig. 1). An exhaustive characterization must therefore consider a wide range of excitation amplitudes, which substantially increases testing time. When considering classical excitation signals such as swept or stepped sines, additional difficulties for the experimental identification of FRCs arise:

*Corresponding author: gaetan.abeloos@uliege.be
[1]Department of Aerospace and Mechanical Engineering, University of Liège, Liège, Belgium
[2]Department of Mechanical Engineering, Imperial College London, London, United Kingdom

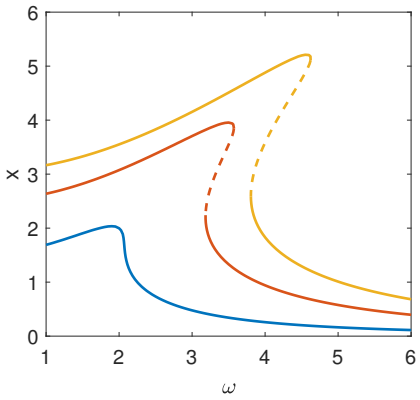

Figure 1: FRCs of the Duffing oscillator: $p = 4$ (——), 14 (——), 24 (——) with stable (——) and unstable (- - -) orbits

- The same excitation signal can lead to distinct steady-state responses of the system, depending on its initial state. If perturbed, the system can also jump from one periodic orbit to another.
- The basin of attraction of a stable branch shrinks when approaching a bifurcation meaning that the system might jump before reaching resonance, leaving it unidentified.
- Periodic orbits can be unstable, i.e., the motion quickly diverges from them and converges toward some other (stable) orbits. The unstable branches are therefore not observable in practice.

These three issues have motivated researchers to develop new approaches to test nonlinear structures in a more systematic and reliable way. One of which is the extension of numerical continuation to a feedback-controlled experiment. The feedback control is used to stabilize an unstable periodic orbit whereas the continuation process is exploited to move smoothly from one orbit to another. Physicists were successful in stabilizing unstable orbits by using time-delayed feedback control [5]. Control-based continuation (CBC) was first proposed by Sieber and Krausskpof [6, 7] to calculate experimental FRCs without the need for a mathematical model of the system at hand. CBC was then used by the engineering community to perform the experimental identification of FRCs of mechanical systems, see e.g. [8, 9, 10].

CBC aims at (i) controlling an experimental parameter θ by comparing it to a reference θ^*, generating the action u of a controller $g(\cdot)$, $u = g(\theta^* - \theta)$, which stabilizes the sought periodic orbit and (ii) varying the reference θ^* during the continuation process to obtain a complete family of periodic orbits. In order to identify orbits of the original system, the controller must be non-invasive, i.e., u must vanish when the system lies on the orbit.

The choice of the controlled parameter θ is thus instrumental in CBC. Because of the folding that occurs at resonance in Fig. 1, the forcing frequency undergoes a non-monotonous increase at constant forcing amplitude. Using the forcing frequency as continuation parameter would thus require advanced continuation schemes. Representing FRCs against the forcing amplitude and the forcing frequency in a three-dimensional plot reveals that the manifold to be identified (in grey in Fig. 2) can be "sliced" at constant forcing frequency (Fig. 2b) instead of constant forcing amplitude (Fig. 2a) to obtain the so-called S-curves. Incidentally, imposing a constant forcing frequency is easier than imposing the amplitude. Fig. 3 evidences the key feature of S-curves, i.e., the system's displacement increases monotonically for a fixed forcing frequency, opening the door to simple continuation schemes. The identification of S-curves with θ^* taken as a reference displacement x^* thus represents an indirect, but effective, way to identify FRCs [11].

This strategy was exploited in several studies, including the following. Backbone curves were identified in [12]. CBC was applied to a structure with harmonically coupled modes in [13], to a frictional structure in [14], a structure vibrating with impacts in [10], and numerically to a biochemical system in [15]. The stability of orbits was evaluated in [16] whereas bifurcations were tracked through frequency, forcing,

and displacement in [17]. The topology of the manifold can also be estimated during the experiment to improve continuation [18].

To understand how the unstable portions of a S-curve can be stabilized using feedback control, a differential controller of gain k_d is applied to the Duffing oscillator. Specifically, the displacement x is compared against a harmonic signal of amplitude x^*:

$$\ddot{x}(t)+\dot{x}(t)+x(t)+x^3(t) = k_\mathrm{d}\frac{\mathrm{d}}{\mathrm{d}t}[x^* \sin\omega t - x(t)]. \quad (2)$$

The terms of Eq. (2) are rearranged to highlight that the differential controller leads to an increase in the damping of the oscillator:

$$\ddot{x}(t)+[1+k_\mathrm{d}]\dot{x}(t)+x(t)+x^3(t) = k_\mathrm{d}x^*\omega\cos\omega t. \quad (3)$$

The controller is applied to the unstable orbit for which $x = 3.5$ and $\omega = 4$ in Fig. 3a. Its basin of attraction in Fig. 3b highlights the existence of two competing stable orbits. Fig. 4a considers three different values of the controller gain k_d. When $k_\mathrm{d} = 0.5$ or 1, the (x,x^*) curve remains unstable for $x = 3.5$; the basins of attraction are given in Figs. 4b and 4c, respectively. When $k_\mathrm{d} = 2$, there is a unique, stable orbit for $x = 3.5$, as confirmed by the basin of attraction in Fig. 4d. At this gain, Fig. 4a evidences a one-to-one relation between the amplitude of the system's response x and the control parameter x^*; a complete unfolding is thus achieved by the differential controller. The corresponding forcing amplitude lies in the right-and side of Eq. (2).

Despite the stabilization of unstable orbits, the controller must also be non-invasive; i.e., the action of the controller must be zero at the sought orbit. This cannot be achieved in Eq. (2) if higher harmonics in x are not considered. One inherent limitation of the current implementations of CBC is that fixed-point iterations [11] (or even quasi-Newton iterations [7, 8]) are necessary to remove the invasiveness of the controller. To do so, the system must reach steady state before doing the corrective iteration. The central contribution of the present study is to introduce a new CBC algorithm which cancels invasiveness online, i.e., without the need for offline iterations, resulting in simpler implementations and faster experiments.

There exist other methods which exploit feedback control to experimentally measure the dynamic response of nonlinear systems. For instance, Phase-locked Loops (PPLs) were proposed in [19, 20] and control the phase lag between the applied excitation and the response of the system. They were used to measure FRCs in [21]. In those applications, PLLs relied on the unique parameterization of the response manifold in terms of the phase lag. PLLs were also used to identify backbone curves on a number of systems including stiffness and friction nonlinearities [22, 23, 24, 25]. FRCs were synthesized from the measured backbones in [21]. Compared to CBC, PLLs are naturally non-invasive methods. However, the control architecture of PLLs is fixed.

Another method which uses feedback control to characterize the response of nonlinear structures is the so-called Response-Controlled stepped-sine Testing (RCT) [26, 27]. CBC and RCT share an important conceptual similarity as both methods directly control the response of the system to achieve a particular response target. However, while CBC usually explores the response of the system at a constant forcing frequency but different response amplitudes, RCT maps the response of the system at a constant response amplitude but different excitation frequencies. As a result, while the response manifold obtained using CBC comprises a collection of S-curves, the response manifold identified using RCT is composed of horizontal slices of the response manifold (in Fig. 2 for instance). FRCs, S-curves and RCT's constant-response FRFs are in fact the three possible ways in which the response manifold can be sliced. Data collected using RCT was interpolated using the Harmonic Force Surface (HFS) concept to successfully identify the nonlinearities of structures with stiffness [26], friction, and backlash [27] nonlinearities. However, RCT neglects the effects of non-fundamental harmonics, leaving the controller invasive and potentially affecting the identified orbits.

The article is organized as follows. The existing

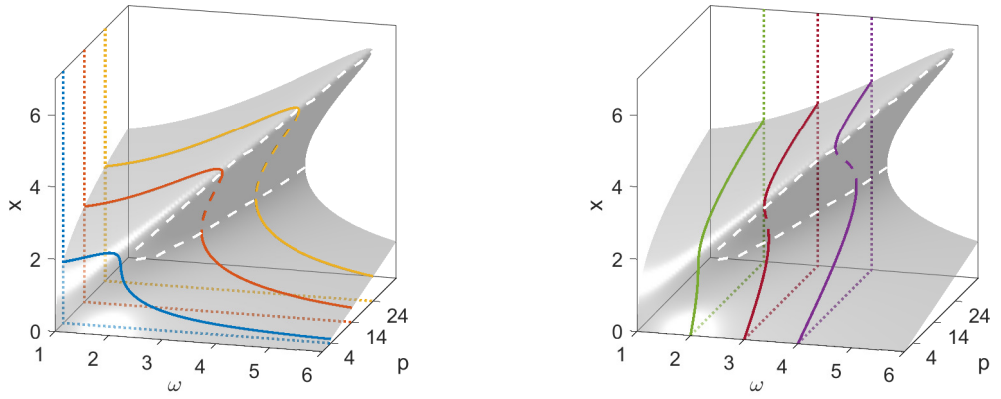

Figure 2: Manifold of the Duffing oscillator linking displacement amplitude x, forcing frequency ω and forcing amplitude p with (a) FRCs at constant excitation amplitudes $p = 4$ (—) , 14 (—), 24 (—) and (b) S-curves at constant frequencies $\omega = 2$ (—), 3 (—), 4 (—); the locus of saddle-node bifurcations is marked by a white dashed line, it represents the boundary between stable and unstable orbits

CBC algorithm, termed offline CBC, is reviewed in Section 2. The proposed online CBC method is presented in Section 3; it relies on the use of adaptive filters derived from a notch filter introduced in [28]. We will show that the method can perform the continuation either by discrete steps or by sweeping the continuation parameter continuously. In Section 4, the algorithm is demonstrated experimentally using a cantilever beam. The three methods, namely offline CBC, stepped CBC and swept CBC, are used to characterize one mode of the beam with various artificial nonlinearities in stiffness and damping. The methods are compared with respect to the efficacy of invasiveness cancellation, accuracy of the characterization, and time.

2 Offline Control-Based Continuation

This article focuses on the dynamics of a one-degree-of-freedom oscillator under monoharmonic forcing. Specifically, the objective is to stabilize the unstable periodic orbits through feedback control which, in turn, allows us to construct the different S-curves defining the manifold of the oscillator.

The conceptual diagram of the feedback control loop is shown in Fig. 5a. Because a nonlinear system responds at different frequencies under monoharmonic forcing, its displacement x can be decomposed into fundamental and non-fundamental harmonic components, i.e., $x(t) = x_{\mathrm{f}}(t) + x_{\mathrm{nf}}(t)$. Likewise, the reference displacement x^* is decomposed into fundamental and non-fundamental harmonic components, i.e., $x^*(t) = x^*_{\mathrm{f}}(t) + x^*_{\mathrm{nf}}(t)$. These different components feed the controller which, in turn, synthesizes an augmented excitation signal $f(t) = f_{\mathrm{f}}(t) + f_{\mathrm{nf}}(t)$. The fundamental component f_{f} represents the monoharmonic excitation applied to the system. The non-fundamental component f_{nf} comprises undesired multiharmonic components, i.e., when $f_{\mathrm{nf}} \neq 0$, the controller is invasive. The invasive action of the controller is therefore expressed

$$f_{\mathrm{nf}}(t) = g(x^*_{\mathrm{nf}} - x_{\mathrm{nf}}). \tag{4}$$

We remark that the practical implementation of

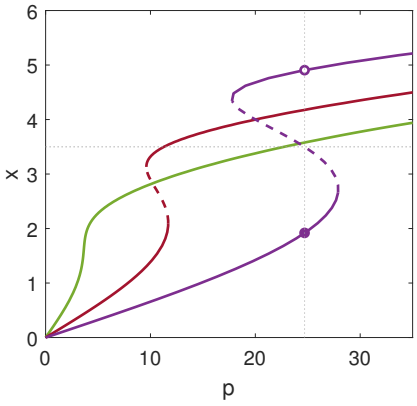

(a)

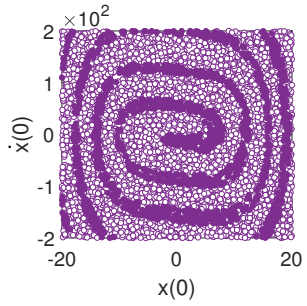

(b)

Figure 3: (a) S-curves for $\omega = 2$ (—), 3 (—), 4 (—) with stable (—) and unstable (- - -) orbits, (b) basin of attraction for $\omega = 4$ and $x = 3.5$ showing the two competing stable orbits (• or ○)

the algorithm schematized in Fig. 5b does not require the explicit separation into fundamental and non-fundamental components. To this end, a linear controller can be used to guarantee the independence of harmonic components such that $f(t) = g(x^* - x)$ is the excitation eventually applied to the system. Specifically, a proportional-derivative (PD) controller is used herein:

$$\begin{aligned} f(t) &= g(x^* - x) \\ &= k_\mathrm{p}[x^*(t) - x(t)] + k_\mathrm{d}[\dot{x}^*(t) - \dot{x}(t)] \end{aligned} \quad (5)$$

where k_p and k_d are the proportional and differential gains, respectively. Similarly to what was illustrated in Eq. (3), the influence of a PD controller can be intuitively understood as adding stiffness (k_p) and damping (k_d) to the system. For adequate gains, the controller modifies the system's dynamics, stabilizes the unstable orbits and unfolds the S-curves.

2.1 Fundamental excitation

The fundamental components of the signals are expressed as a function of their Fourier coefficients:

$$x_\mathrm{f}(t) = X_\mathrm{1s}\sin(\omega t) + X_\mathrm{1c}\cos(\omega t) \quad (6)$$
$$x^*_\mathrm{f}(t) = X^*_\mathrm{1s}\sin(\omega t) + X^*_\mathrm{1c}\cos(\omega t) \quad (7)$$
$$f_\mathrm{f}(t) = F_\mathrm{1s}\sin(\omega t) + F_\mathrm{1c}\cos(\omega t). \quad (8)$$

The relation between them is expressed from Eq. (5)

$$\begin{cases} F_\mathrm{1s} = k_\mathrm{p}(X^*_\mathrm{1s} - X_\mathrm{1s}) - \omega k_\mathrm{d}(X^*_\mathrm{1c} - X_\mathrm{1c}) \\ F_\mathrm{1c} = k_\mathrm{p}(X^*_\mathrm{1c} - X_\mathrm{1c}) + \omega k_\mathrm{d}(X^*_\mathrm{1s} - X_\mathrm{1s}). \end{cases} \quad (9)$$

The fundamental components of the displacement and reference signals therefore generate the fundamental excitation applied to the system. The fundamental amplitudes of the signals are expressed as

$$X_\mathrm{f} = \sqrt{{X_\mathrm{1s}}^2 + {X_\mathrm{1c}}^2} \quad (10)$$
$$X^*_\mathrm{f} = \sqrt{{X^*_\mathrm{1s}}^2 + {X^*_\mathrm{1c}}^2} \quad (11)$$
$$F_\mathrm{f} = \sqrt{{F_\mathrm{1s}}^2 + {F_\mathrm{1c}}^2}. \quad (12)$$

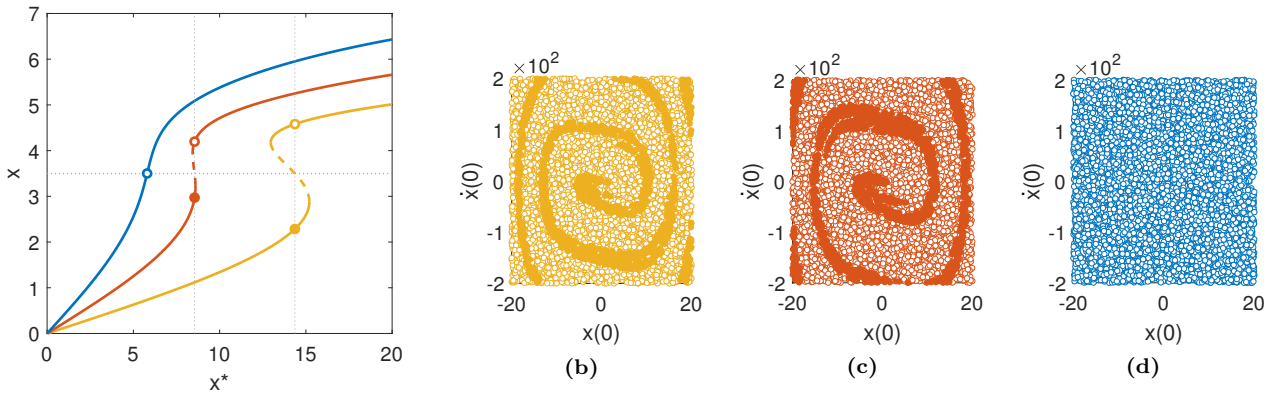

Figure 4: (a) S-curves for $\omega = 4$ and $k_\mathrm{d} = 0.5$ (—), 1 (—), or 2 (—) with stable (—) and unstable (- - -) orbits; (b-d) basins of attraction for $x = 3.5$ showing which stable orbit (• or ∘) is reached

2.2 Invasiveness of the controller

The non-fundamental components of the signals are decomposed in Fourier series:

$$x_\mathrm{nf}(t) = X_0 + \sum_{k=2}^{N_\mathrm{H}} X_{ks}\sin(k\omega t) + X_{kc}\cos(k\omega t) \quad (13)$$

$$x^*_\mathrm{nf}(t) = X^*_0 + \sum_{k=2}^{N_\mathrm{H}} X^*_{ks}\sin(k\omega t) + X^*_{kc}\cos(k\omega t) \quad (14)$$

$$f_\mathrm{nf}(t) = F_0 + \sum_{k=2}^{N_\mathrm{H}} F_{ks}\sin(k\omega t) + F_{kc}\cos(k\omega t), \quad (15)$$

the relation between them is expressed from Eq. (5) $\forall k \in \{2, \ldots, N_\mathrm{H}\}$

$$\begin{cases} F_0 = k_\mathrm{p}(X^*_0 - X_0) \\ F_{ks} = k_\mathrm{p}(X^*_{ks} - X_{ks}) - k\omega k_\mathrm{d}(X^*_{kc} - X_{kc}) \\ F_{kc} = k_\mathrm{p}(X^*_{kc} - X_{kc}) + k\omega k_\mathrm{d}(X^*_{ks} - X_{ks}). \end{cases} \quad (16)$$

Because a nonlinear system generates harmonics that are not known beforehand, F_{ks} and F_{kc} are non-zero, and so is $f_\mathrm{nf}(t)$. As a result, the controller is invasive and causes the excitation force $f(t)$ to contain multiple harmonic components. This means that the system follows a periodic orbit that does not belong to the sought manifold.

Eq. (16) shows that modifying the reference x^*_nf until it is equal to x_nf is a way to render the control non-invasive:

$$\begin{cases} X^*_0 = X_0 \\ X^*_{ks} = X_{ks} \\ X^*_{kc} = X_{kc} \end{cases} \Leftrightarrow \begin{cases} F_0 = 0 \\ F_{ks} = 0 \\ F_{kc} = 0 \end{cases} \qquad \forall k \in \{2, \ldots, N_\mathrm{H}\}. \quad (17)$$

To cancel the invasiveness of the controller, current implementations of CBC thus iteratively correct the Fourier coefficients of the reference signal x^* to achieve Eq. (17) [11].

2.3 The offline CBC algorithm

The complete CBC algorithm is illustrated in Fig. 6a where the feedback loop of Fig. 5b lies in the gray area and the updating of the Fourier coefficients (17) is made outside this area. For the stability of the system to change, the feedback loop must run continuously through time representing the **online part** of the method. The correction step must be achieved

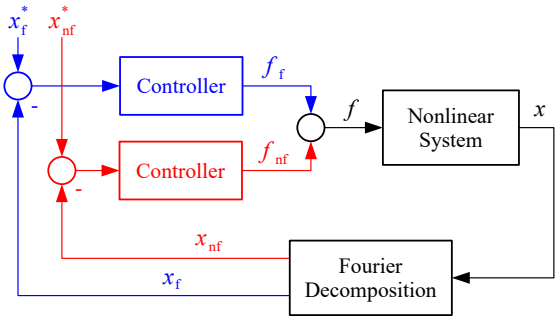

(a)

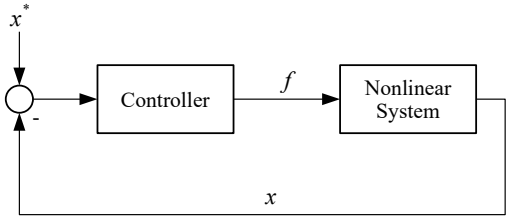

(b)

Figure 5: CBC feedback loop with (a) the separation of fundamental (——) and non-fundamental (——) components and (b) actual implementation of the algorithm

when the system is in steady state; it is thus the **offline part** of the method, hence the name offline CBC algorithm.

The process starts with the initialization of the Fourier coefficients of x^* to generate a monoharmonic signal of arbitrarily small amplitude $X^*_{1s,0}$ and frequency ω_0. When the system is at steady state, the corrective iterations on the non-fundamental Fourier coefficients of x^* are performed. This iterative process goes on until the control is non-invasive. Once this is the case, a periodic solution on the sought S-curve has been identified. We note that the fundamental Fourier coefficients X^*_{1s} and X^*_{1c} are never modified during the iterations. They define the fundamental reference amplitude X^*_f. Eq. (9) shows how these coefficients implicitly set the fundamental response amplitude X_f of the system.

To identify a new periodic solution on the S-curve, X^*_f is incremented through $X^*_{1s} := X^*_{1s} + h$, performing in essence what is referred to as sequential continuation in the literature. Once a complete S-curve has been identified, the continuation process is repeated for a different frequency ω. Eventually, the manifold in Fig. 2 can be constructed and subsequently sliced at constant forcing amplitudes to calculate the FRCs.

3 Online control-based-continuation

The key idea of this article is to impose Eq. (17) online. Specifically, the synthesis of x^*_{nf} can be achieved by an online estimation of the Fourier coefficients of x through adaptive notch filters [28].

3.1 Adaptive filtering

An adaptive filter synthesizes the signal $\hat{x}$ by performing a time-varying linear combination of a basis

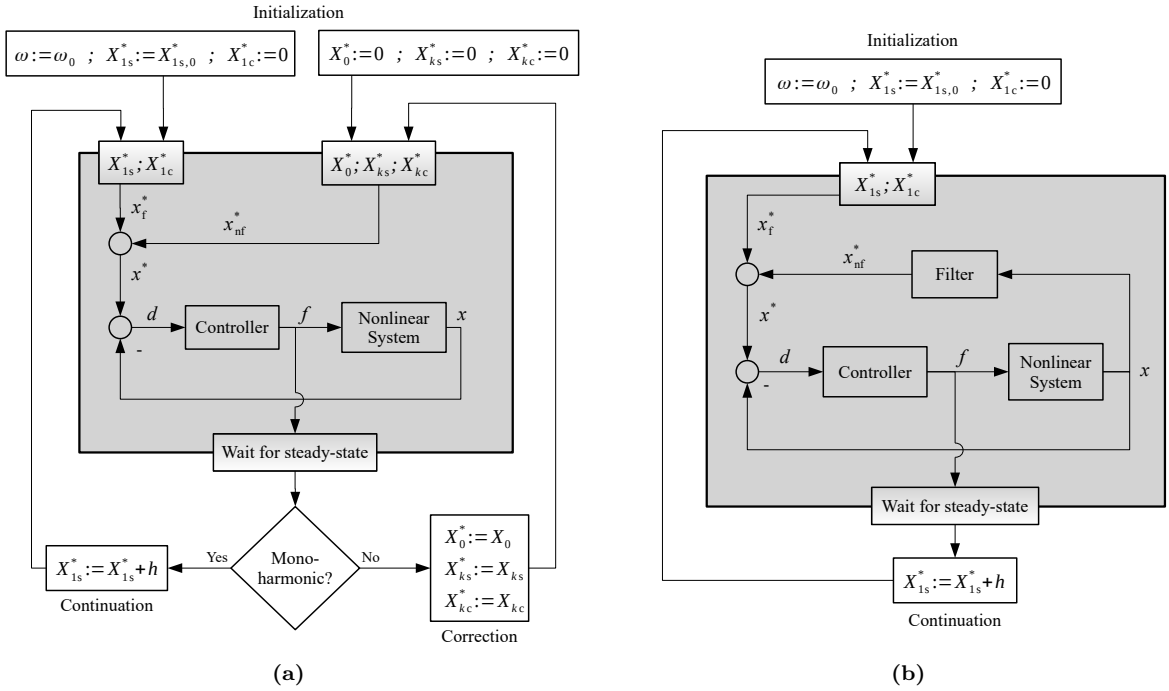

Figure 6: Comparison of the (a) offline and (b) online CBC algorithms for the identification of an S-curve. The gray area represents the online steps of the algorithms.

$\mathbf{q}$ such that it approximates the measured signal x:

$$\hat{x}(t) = \mathbf{w}^T(t)\mathbf{q}(t) \approx x(t). \tag{18}$$

The basis $\mathbf{q}$ is composed of harmonic signals

$$\mathbf{q}(t) = \begin{bmatrix} q_0(t) \\ q_{1\mathrm{s}}(t) \\ q_{1\mathrm{c}}(t) \\ q_{2\mathrm{s}}(t) \\ \vdots \\ q_{N_{\mathrm{H}}\mathrm{c}}(t) \end{bmatrix} = \begin{bmatrix} 1 \\ \sin(\omega t) \\ \cos(\omega t) \\ \sin(2\omega t) \\ \vdots \\ \cos(N_{\mathrm{H}}\omega t) \end{bmatrix} \tag{19}$$

and the combination coefficients are the weights

$$\mathbf{w}(t) = \begin{bmatrix} w_0(t) \\ w_{1\mathrm{s}}(t) \\ w_{1\mathrm{c}}(t) \\ w_{2\mathrm{s}}(t) \\ \vdots \\ w_{N_{\mathrm{H}}\mathrm{c}}(t) \end{bmatrix}. \tag{20}$$

When the synthesis error $\epsilon = x - \hat{x}$ and the time variation of the weights $\mathbf{w}$ are small, Eq. (18) is similar to a Fourier decomposition of x and the elements of $\mathbf{w}$ approximate its Fourier coefficients:

$$\begin{cases} w_0 \approx X_0 \\ w_{k\mathrm{s}} \approx X_{k\mathrm{s}} \\ w_{k\mathrm{c}} \approx X_{k\mathrm{c}} \end{cases} \quad \forall k \in \{1, \ldots, N_{\mathrm{H}}\}. \tag{21}$$

Any harmonic component can be selected from $\mathbf{q}$. In particular, the identified non-fundamental harmonic components and their corresponding weights can be used to synthesize

$$x^*_{\mathrm{nf}}(t) = \mathbf{w}^T_{\mathrm{nf}}(t)\mathbf{q}_{\mathrm{nf}}(t) \approx x_{\mathrm{nf}}(t) \tag{22}$$

meeting the objective in Eq. (17).

There exist several adaptive filtering algorithms. The simplest and least expensive is the least mean squares (LMS) algorithm, which updates $\mathbf{w}$ discretely through time. At time step i, the synthesis error is estimated, $\epsilon(t_i) = x(t_i) - \mathbf{w}^T(t_i)\mathbf{q}(t_i)$, and the weights are updated accordingly

$$\mathbf{w}(t_{i+1}) = \mathbf{w}(t_i) + \mu\mathbf{q}(t_i)\epsilon(t_i) \tag{23}$$

where μ is the step size factor, which is an internal parameter of the LMS algorithm. For further information about adaptive filters, the reader is invited to consult reference books, e.g. [29].

3.2 The online CBC algorithm

The resulting algorithm is shown in Fig. 6b. It is seen that the identification of a periodic solution on the S-curve can continuously run through time. The method is thus referred to as online CBC.

To build the complete S-curve, there are two options for the continuation step. The first alternative is to perform offline a sequential continuation on the fundamental amplitude X^*_{f} through $X^*_{1\mathrm{s}} := X^*_{1\mathrm{s}} + h$, as for the offline CBC algorithm. The second possibility is to impose a time-varying fundamental reference amplitude $X^*_{\mathrm{f}}(t) = \eta t$ in the online part of Fig. 6b. The two methods are referred to as stepped and swept CBC, respectively.

The advantage of swept CBC is that it requires no offline action which can speed up the identification of a S-curve. However, depending on the sweep rate η, this can come at the expense of accuracy.

4 Experimental validation

The proposed online CBC algorithms are demonstrated experimentally on a cantilever beam including various artificial nonlinearities in this section.

4.1 Experimental set-up

The experimental set-up in Fig. 7a comprised a cantilever steel beam excited by an electrodynamic shaker. Its displacement was measured by a laser vibrometer to form a single-input single-output (SISO) system.

The beam and its base in Fig. 7b were made from a single block of metal in order to avoid micro-slips in the beam-base connection. The absence of micro-slips renders the physical structure as linear as possible so that nonlinear behavior comes predominantly from the artificial nonlinearity. Furthermore, the absence of bolts between the beam and the base is expected to improve repeatability. The base was bolted to the ground. The dimensions of the beam are listed in Table 1. The electrodynamic shaker (TIRA TV 51075) was connected perpendicularly to the beam at 30 cm from the base through a stinger and an impedance head (DYTRAN 5860B) glued to the surface, see Fig. 7c.

The different nonlinearities were realized using the real-time controller (RTC) dSPACE MicroLabBox. The force applied by the shaker to the structure was $f_{\text{shaker}}(t) = f(t) - f_{\text{nl}}(x, \dot{x})$ where $f(t)$ is the external force and f_{nl} is the artificial nonlinearity. The RTC sent the excitation signal as a voltage, transformed in current by the power amplifier (TIRA BAA 120). The current then ran through the shaker's coils, generating a force on the magnetic core attached to the casing by a membrane. For the generation of the artificial nonlinearities, it is important that the force applied to the physical system corresponds to the signal sent by the RTC. It is non-trivial to impose an exact force signal at the impedance head, whereas the force inside the shaker is proportional to the current running through its coil. For this reason, the physical system includes the impedance head, the stinger, the magnetic core, and the shaker's membrane in addition to the beam. The excitation point is therefore the shaker's magnetic core. Under 20 Hz, a non-constant transfer function between the input voltage of the shaker's amplifier and its output current is observed. In this case, the artificial nonlinearity cannot be implemented. Consequently, only modes above 20 Hz can be studied. The proportionality constant between the force applied to the core and the RTC's output was measured to be 160 N/V.

The laser vibrometer (Polytec NLV-2500-5) measured the displacement and velocity of the magnetic core so that the excitation and measurement points were collocated. The displacement and velocity signals were then sent to the RTC for the calculation of the artificial nonlinearities.

Table 1: Dimensions of the cantilever steel beam [cm]

Length	Width	Height
100	0.6	2

Table 2: Natural frequencies ω_n and damping ratios ξ of the physical system's first 6 modes

Mode	ω_n [Hz]	ξ [%]
1	6.2	0.82
2	31.8	0.66
3	78.3	0.35
4	170.9	0.13
5	254.6	1.24
6	303.5	0.56

4.2 Experimental characterization of the linear beam

The beam was excited by sine sweeps at a low amplitude of 0.3 N without artificial nonlinearity in order to obtain its linear frequency response function (FRF). The PolyMAX method [30] identified the modal parameters of the first six modes in Table 2. The FRF was then expressed as a linear combination of six single-pole transfer functions, each corresponding to a mode. The single-pole transfer functions' gains were computed such that the amplitude of their sum at resonance corresponds to the measurement. A linear mass-spring-damper model of the beam was also established. The measured and synthesized FRFs are compared in Fig. 8.

CBC will be applied in the next sections to the third mode of the beam whose natural frequency is around 80 Hz. This mode is targeted because, as discussed above, the implementation of the artificial nonlinearity necessitates a constant transfer function between the shaker's voltage and force. Despite that a single mode was targeted, we note that the multi-

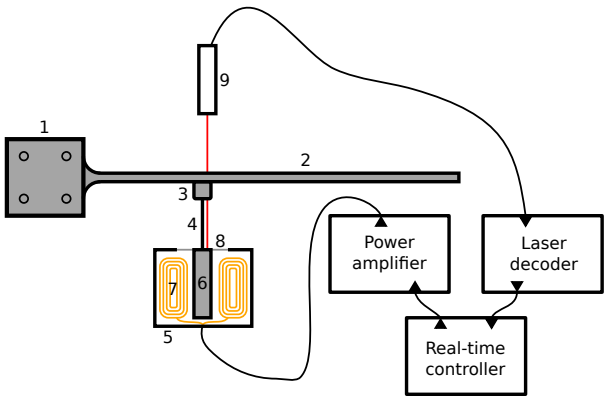

(a)

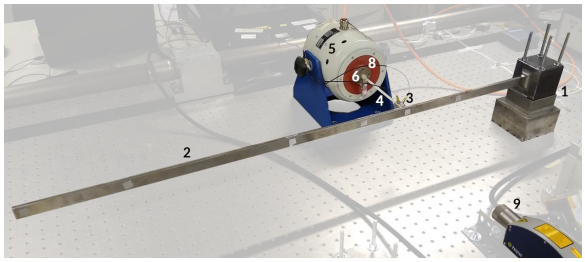

(b)

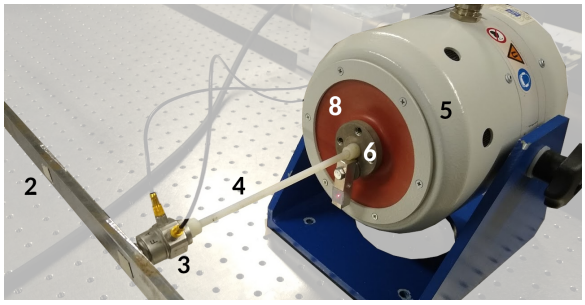

(c)

Figure 7: Experimental setup composed of: (1) fixed base, (2) cantilever beam, (3) impedance head, (4) stinger, (5) shaker's casing, (6) shaker's magnetic core, (7) shaker's electrical coils, (8) shaker's membrane, (9) laser vibrometer.

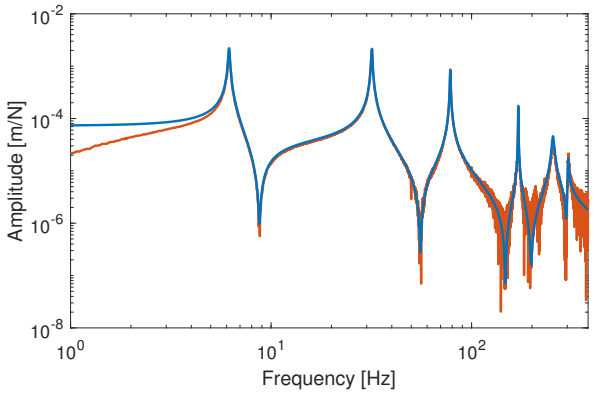

Figure 8: FRFs of the linear beam: measured (—) and synthesized from the mass-spring-damper model (—)

mode model described above was necessary to validate the results and handle potential modal interactions, a phenomenon studied in [31]. When the excitation level was increased to 0.5 N in Fig. 9, this mode exhibited a slight softening behavior. The nonlinearity

$$f_{\mathrm{nl,model}}(x,\dot{x}) = k_{\mathrm{stif}}\, x^2\, \mathrm{sgn}(x) + k_{\mathrm{damp}}\, \dot{x}^2\, \mathrm{sgn}(\dot{x}), \quad (24)$$

was therefore included in the identified linear model with $k_{\mathrm{stif}} = -2.7 \times 10^6$ N/m^2 and $k_{\mathrm{damp}} = -1.2$ Ns^2/m^2 manually defined to fit the experimental FRC visually. A proper nonlinear model identification is feasible but not necessary in this work.

4.3 Identification of a Duffing oscillator

The first artificial nonlinearity considered to demonstrate the CBC algorithms is a cubic stiffness:

$$f_{\mathrm{nl},1}(x) = k_3\, x^3, \quad (25)$$

where $k_3 = 3 \times 10^{11}$ N/m^3. The offline, stepped and swept strategies were applied to this Duffing oscilla-

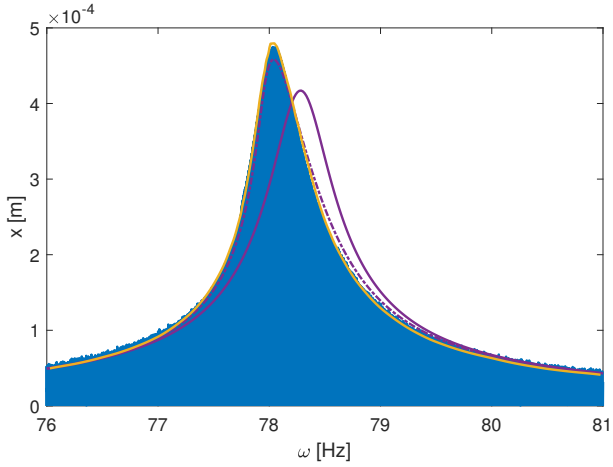

Figure 9: Characterization of the physical system without artificial nonlinearity with FRC at 0.5 N obtained by open-loop frequency sweep (——), the linear model (——), the corrected model (– · –), and the dynamic manifold (——)

tor.

As of today, there is no general method to design an appropriate controller for CBC. This subject is an active area of research, e.g. a recent study developed adaptive control schemes for the stabilization of equilibrium points of linear systems using CBC [32]. In the absence of such a method for the application at hand, a differential controller was used throughout this study. Its gain k_d was chosen by trial and error and by allowing the structure to jump between two stable solutions. If there were jumps during the continuation, the gain was too low, as illustrated in Fig. 4. In this case, the gain was simply increased until there were no more jumps during the continuation. Interestingly, it was found that a high differential gain consistently leads to better stabilization. The stability bound of this tendency was not explored. A gain $k_\mathrm{d} = 400$ Ns/m was quickly found to be adequate for stabilizing the different nonlinear systems.

The user-defined parameters are listed in Table 3. Five harmonics were considered for all CBC strategies and a 10 kHz sampling frequency was sufficient for measuring them properly. The step size h for the offline and stepped methods was chosen to obtain approximately 50 measurement points on the S-curves, a good compromise between short testing time and sufficient refinement of the S-curves for manifold interpolation. The sweep rate η for the swept continuation was such that the testing time was significantly shorter than with the other strategies.

The steady-state detection algorithm illustrated in Fig. 10 was implemented for the offline and stepped methods. The Fourier coefficients of the displacement signal are estimated after each period. A buffer collects the evolution of the coefficients over 5 periods and computes their standard deviations. The greatest standard deviation among the Fourier coefficients ("max std(X)") defines the convergence indicator that is compared to an absolute tolerance $\mathrm{tol}_\mathrm{conv,a}$. Because of transients, this indicator is evaluated after each interval of 10 periods. Similarly, the greatest non-fundamental Fourier coefficient of the force signal ("max $|F_\mathrm{nf}|$") defines an invasiveness indicator that is used for the offline method. Because the amplitude of the force varies greatly along an S-curve, this indicator is compared to an absolute tolerance $\mathrm{tol}_\mathrm{inv,a}$ and its ratio to the fundamental amplitude is compared to a relative tolerance $\mathrm{tol}_\mathrm{inv,r}$. For the stepped and swept methods, the internal parameter μ of the LMS algorithm in Eq. (23) depends strongly on the sampling frequency and its normalized value is listed in Table 3.

The S-curves obtained by the different algorithms are displayed in Fig. 11. The curves slightly differ depending on the invasiveness of the controller, i.e., on the non-fundamental Fourier coefficients remaining in the excitation signal. The effect is particularly important near resonance, arguably the most critical point of the S-curve. The offline and stepped methods are however in very good agreement. The transient effects related to the swept method are responsible for a somewhat greater discrepancy in the measured S-curve.

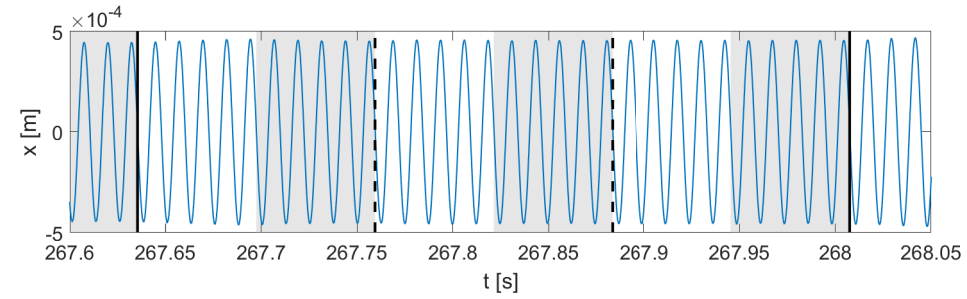

(a)

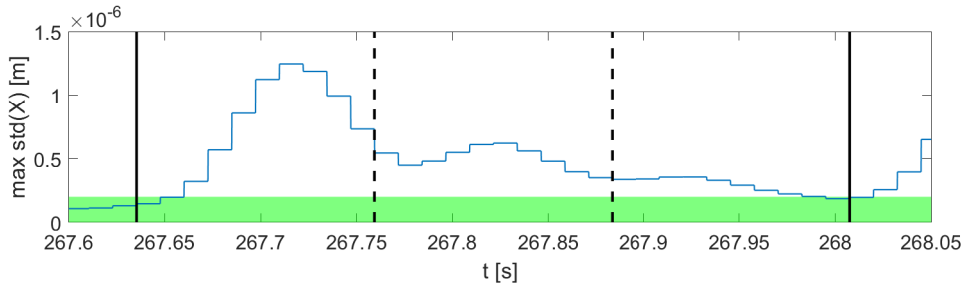

(b)

Figure 10: Steady-state detection algorithm: (a) time series of the displacement with evaluation of steady-state every 10 periods (- - -) and with continuation steps (——) when the indicator is below the tolerance and (b) convergence indicator computed every period over buffers of 5 periods (▬) with the tolerance $\mathrm{tol}_{\mathrm{conv,a}}$ (▬)

To have a more precise view of the invasiveness of the different schemes, Fig. 12 depicts the evolution of the maximum Fourier coefficient of f_{nf}. Without invasiveness cancellation, this coefficient rises above 1 N whereas it is reduced by more than one order of magnitude with cancellation. The offline method is able to reduce $\max|F_{\mathrm{nf}}|$ down to two orders of magnitude by performing corrective iterations. More iterations lead to lower values, but $\max|F_{\mathrm{nf}}|$ increases significantly after each continuation step, rendering correction necessary. The stepped method cannot reduce $\max|F_{\mathrm{nf}}|$ below twice what is achieved with the offline method highlighting that there is a limit to the performance of adaptive filtering depending on the parameter μ. Due to transient effects, the swept method reaches values of $\max|F_{\mathrm{nf}}|$ up to twice what is obtained by the stepped method.

By collecting S-curves measured at different frequencies, the response manifold can be constructed and interpolated by kriging [33], a relatively inexpensive method capable of addressing noise in the data (kriging was used online in [18]). The manifold of the Duffing oscillator is shown in Fig. 13. The resemblance with the manifold in Fig. 2b can be noticed. The manifold can then be sliced at constant excitation amplitudes to extract the FRCs in Fig. 14. For comparison, this figure also includes numerical FRCs calculated using harmonic balance [34] on the model developed in Sect. 4.2 together with the FRCs measured using classical up and down sine sweeps.

The FRCs obtained by offline and stepped CBC are indistinguishable whereas the FRC given by swept CBC exhibits a slight discrepancy near the resonance

Table 3: Parameters of the different CBC strategies: (a) offline, (b) stepped, (c) swept

(a)

h [m]	interval [#per]	buffer [#per]
1×10^{-5}	10	5
$\text{tol}_{\text{inv,a}}$ [N]	$\text{tol}_{\text{inv,r}}$ [%]	$\text{tol}_{\text{conv,a}}$ [m]
0.01	1	2×10^{-7}

(b)

h [m]	interval [#per]	buffer [#per]
1×10^{-5}	10	5
$\text{tol}_{\text{conv,a}}$ [m]	μ [-]	
2×10^{-7}	$10/f_{\text{s}}$	

(c)

η [m/s]	μ [-]
4×10^{-5}	$10/f_{\text{s}}$

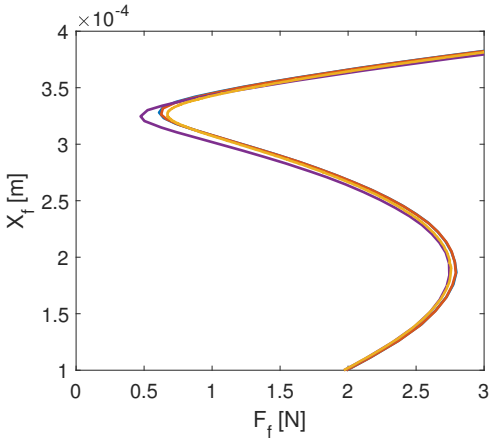

Figure 11: S-curve of the Duffing oscillator at 83.25 Hz: no corrections (—), offline (—), stepped (—), and swept (—)

Table 4: Time in [mm:ss] to identify the S-curve at 83.25 Hz and manifold of the Duffing oscillator

Algorithm	S-curve	Manifold
Swept	00:13	07:09
No cancellation	00.17	—
Stepped	00:18	10:14
Offline	00:32	14:29

peak. They all correlate very well with the displacement amplitude obtained under open-loop sine sweeps. However, as the sweep up approaches the fold bifurcation near resonance, the system jumps prematurely with the result that the sine sweep excitation cannot identify the periodic orbits close to resonance. This result nicely evidences the practical relevance of CBC.

The testing time required for the identification of the S-curve and of the manifold is listed in Table 4. It heavily depends on the duration of transients in the system's response, themselves depending on the CBC controller. Because transients last for a certain number of periods, they are expected to be shorter when identifying a mode around 80 Hz than modes at lower frequencies. Consequently, the absolute duration of the experiments should not be directly compared to performance in the literature. Rather, the relative performance of the online CBC and swept CBC can be compared herein to the state-of-the-art offline CBC. As anticipated, the swept CBC method is the fastest. Interestingly, the stepped method is almost as fast as the algorithm with no corrective action. It stems from the fact that both methods must wait for steady-state before performing the continuation. The offline method is the slowest algorithm and requires roughly twice the time needed for the swept method.

4.4 Other artificial nonlinearities

Other artificial nonlinearities which generate different harmonic contents in the displacement signal are now considered.

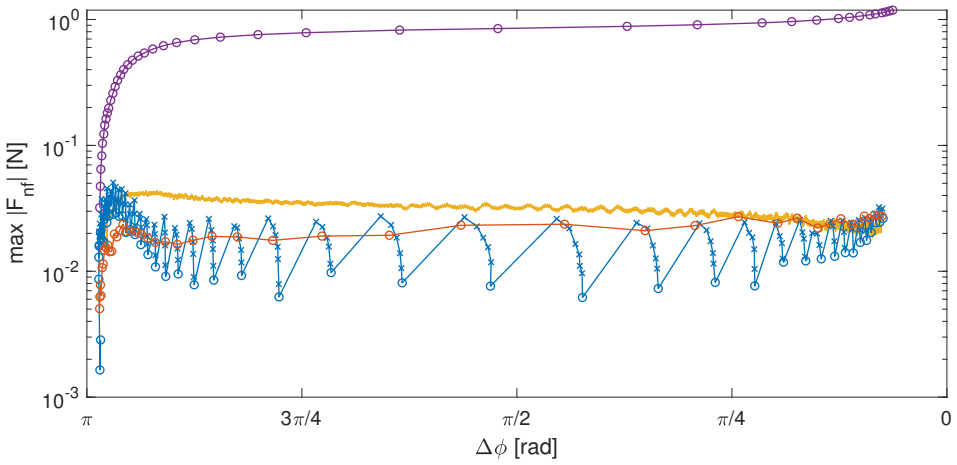

Figure 12: Invasiveness indicator at 83.25 Hz: no corrections (—), offline (—), stepped (—) and swept (—); correction and continuation steps marked with (×) and (○) respectively; phase lag $\Delta\phi$ between X_f and F_f indicating the progression along the S-curve

The identification of a system with hardening-softening-hardening stiffness

$$f_{\mathrm{nl},2}(x) = k_2\ x^2\ \mathrm{sgn}(x) + k_3\ x^3 + k_4\ x^4\ \mathrm{sgn}(x) \quad (26)$$

with $k_2 = 10^8$ N/m^2, $k_3 = -2 \times 10^{11}$ N/m^3, and $k_4 = 10^{14}$ N/m^4 is shown in Fig. 15. The hardening at low and high displacement amplitudes was implemented to avoid negative stiffness in the beam. One can notice the existence of four bifurcation points in the FRC, rendering the open-loop identification much more challenging.

The capability of CBC to characterize a system with non-smooth nonlinearity is demonstrated by introducing a piece-wise linear stiffness

$$f_{\mathrm{nl},3}(x) = \begin{cases} k_{\mathrm{pwl}}(x + x_{\mathrm{lim}}) & \text{for } x \leq -x_{\mathrm{lim}}, \\ 0 & \text{for } -x_{\mathrm{lim}} < x < x_{\mathrm{lim}}, \\ k_{\mathrm{pwl}}(x - x_{\mathrm{lim}}) & \text{for } x \geq x_{\mathrm{lim}}, \end{cases} \quad (27)$$

with $x_{\mathrm{lim}} = 3 \times 10^{-4}$ m and $k_{\mathrm{pwl}} = 3 \times 10^4$ N/m. The manifold (and thus the FRC) in Fig. 16 changes suddenly when reaching the displacement amplitude x_{lim}.

Fig. 17 presents the CBC results when quadratic damping is added to a cubic stiffness:

$$f_{\mathrm{nl},4}(x, \dot{x}) = k_3\ x^3 + k_{\mathrm{qd}}\ \dot{x}^2\ \mathrm{sgn}(\dot{x}) \quad (28)$$

with $k_3 = 3 \times 10^{11}$ N/m^3 and $k_{\mathrm{qd}} = 20$ Ns^2/m^2. The FRCs for a lower excitation level are included to illustrate the change in damping with amplitude.

Finally, friction is added to a cubic stiffness

$$f_{\mathrm{nl},5}(x, \dot{x}) = k_3\ x^3 + \begin{cases} -k_{\mathrm{frict}} & \text{for } \dot{x} < 0 \\ 0 & \text{for } \dot{x} = 0 \\ k_{\mathrm{frict}} & \text{for } \dot{x} > 0 \end{cases} \quad (29)$$

with $k_3 = 3 \times 10^{11}$ n/m^3 and $k_{\mathrm{frict}} = 0.5$ N. The CBC results are given in Fig. 18. The lower amplitude FRCs show that, unlike quadratic damping, the effect of friction is independent of the excitation amplitude.

The testing time to identify the different manifolds is shown in Table 5. Consistent results are observed, namely the swept CBC is the fastest algorithm followed by stepped CBC and then by the offline CBC. It is also seen that the gain in time depends on the

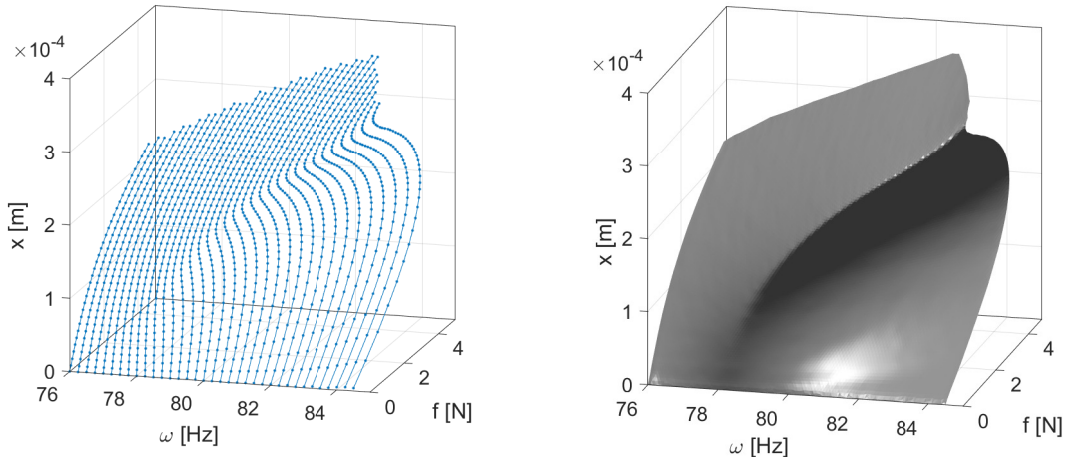

Figure 13: Duffing oscillator identified by the stepped algorithm (a) S-curves measured around the third mode, and (b) manifold interpolated from the S-curves

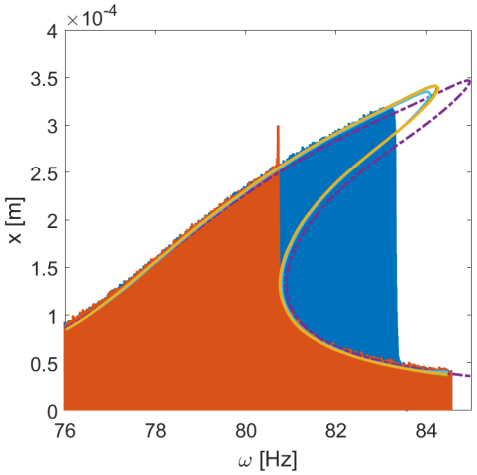

Figure 14: FRCs of the Duffing oscillator at 1N forcing: open-loop sweep up (—) and down (—), calculated from the model (-·-), offline CBC (—), stepped CBC (—) and swept CBC (—)

Table 5: Time in [mm:ss] for the identification of the manifold with cubic stiffness (1), hardening-softening-hardening stiffness (2), piece-wise linear stiffness (3), quadratic damping and cubic stiffness (4), and friction and cubic stiffness (5)

	System				
Algorithm	1	2	3	4	5
Swept	07:09	04:22	06:51	05:18	04:38
Stepped	10:14	08:40	10:23	06:19	06:04
Offline	14:29	10:09	11:55	09:18	09:06

type of nonlinearity. For instance, the softening and piece-wise nonlinearities might increase the duration of the transients, which could explain the greater difference between swept and stepped CBC for those nonlinearities.

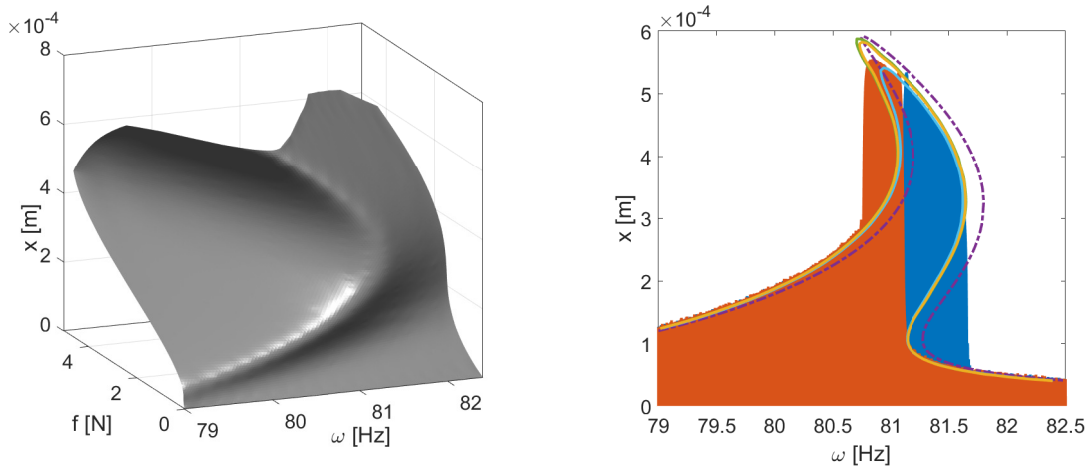

(a) **(b)**

Figure 15: Hardening-softening-hardening stiffness (a) manifold identified with stepped CBC, and (b) FRC at $F = 0.6$ N, open-loop sweep up (—) and down (—), calculated from the model (-·-), offline CBC (—), stepped CBC (—) and swept CBC (—)

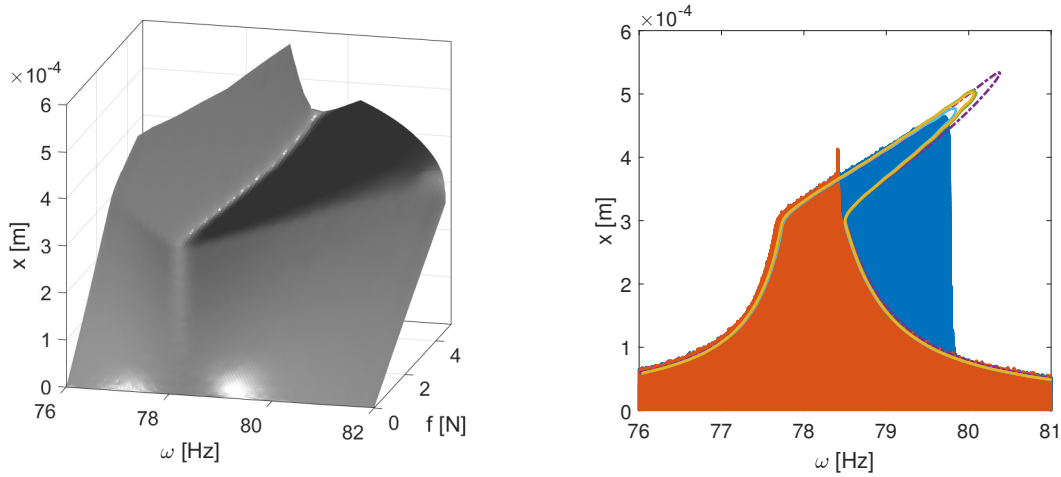

(a) **(b)**

Figure 16: Piece-wise linear stiffness (a) manifold identified with stepped CBC, and (b) FRC at $F = 0.6$ N, open-loop sweep up (—) and down (—), calculated from the model (-·-), offline CBC (—), stepped CBC (—) and swept CBC (—)

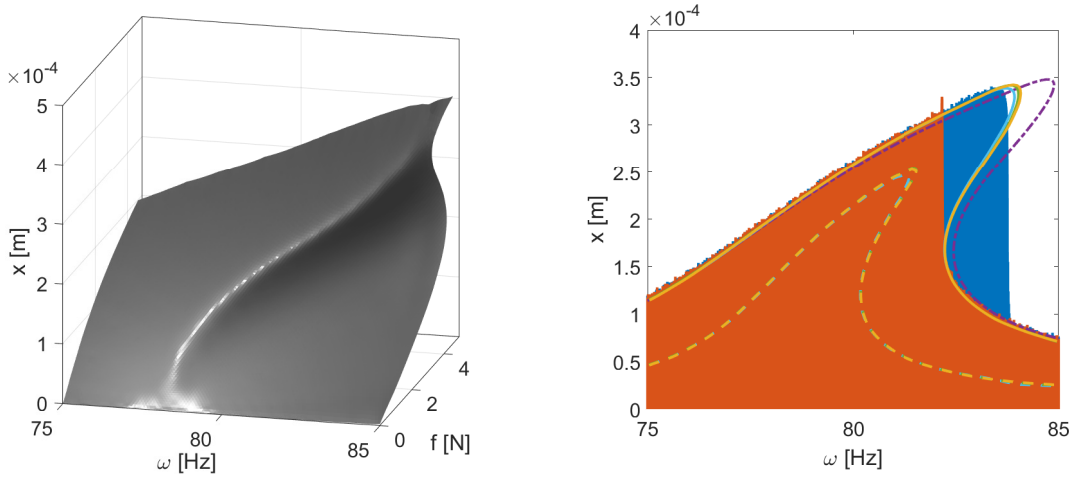

Figure 17: Quadratic damping and cubic stiffness (a) manifold identified with stepped CBC, and (b) FRC at $F = 2$ N, open-loop sweep up (——) and down (——), calculated from the model (-·-·-), offline CBC (——), stepped CBC (——) and swept CBC (——); FRC at $F = 0.7$ N (- - -) obtained by CBC

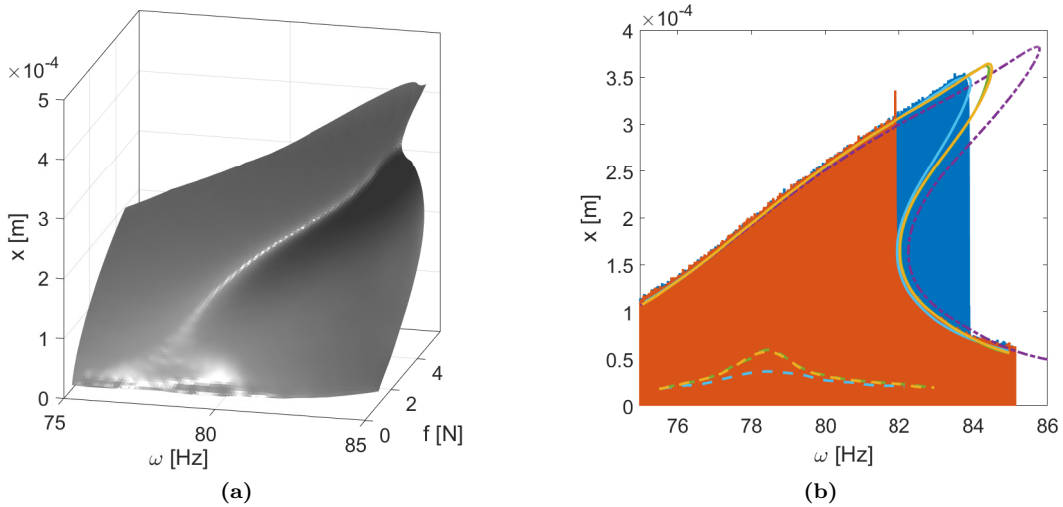

Figure 18: Friction and cubic stiffness (a) manifold identified with stepped CBC, and (b) FRC at $F = 2$ N, open-loop sweep up (——) and down (——), calculated from the model (-·-·-), offline CBC (——), stepped CBC (——) and swept CBC (——); FRC at $F = 0.7$ N (- - -) obtained by CBC

5 Conclusion

The objective of this paper was to exploit adaptive filtering to remove the need for offline corrective iterations during the identification of stable and unstable periodic orbits of nonlinear systems. Two different strategies, termed stepped and swept CBC, were proposed for performing the continuation sequentially or through the sweep of the continuation parameter, respectively.

Both methods are simpler to implement and run faster than the classical, offline CBC; they also require less user-defined parameters. The experimental results obtained using different artificial nonlinearities demonstrated that stepped CBC gives results which correlate very well with those obtained using offline CBC. It should, however, be noted that the offline algorithm can reduce the controller invasiveness up to measurement precision whereas the invasiveness cancellation of the stepped CBC may be limited by the performance of the adaptive filter. Swept CBC cannot reduce invasiveness to the same extent but offers a much shorter running time. Swept CBC represents a very promising nonlinear counterpart of sine sweep testing which is routinely used in industry.

Further work needs to address the design of the CBC controller, and more specifically the choice of the gains and its interaction with adaptive filtering.

An interesting perspective of adaptive filters for the online Fourier decomposition of multiharmonic signals is their application to other experimental methods than CBC. For instance, an adaptive filter can be used in the phase-locked loop methods for the evaluation of the phase lag between the excitation and the response signal's fundamental harmonic.

Declarations

Acknowledgements

G.A. is grateful to the F.R.S.-FNRS for funding this research by the FRIA grant. L.R. acknowledges the financial support of the Royal Academy of Engineering, Research Fellowship #RF1516/15/11.

Funding

This research was funded by the Fond de la Recherche Scientifique (F.R.S.-FNRS) under the Fonds pour la Formation à la Recherche dans l'Industrie et l'Agriculture (FRIA) grant.

Conflict of interest

The authors declare that they have no conflict of interest.

Availability of data and material

The data collected and used in this research will be available at the University of Liège Open Repository and Bibliography (ORBi).

Code availability

The Simulink files used for the experiments and the post-processing scripts will be available at the University of Liège Open Repository and Bibliography (ORBi).

References

[1] H. B. Keller. Numerical solution of bifurcation and nonlinear eigenvalue problems. In P. Rabinowitz, editor, *Applications of Bifurcation Theory*, pages 359–384. Academic Press, New York, 1977.

[2] R Seydel. A continuation algorithm with step control. In *Numerical methods for bifurcation problems*, pages 480–494. Springer, 1984.

[3] E Doedel and J Kernévez. Auto: Software for continuation problems in ordinary differential equations with applications. *Applied Mathematics, California Institute of Technology, Pasadena, CA*, 1986.

[4] Ali H Nayfeh and Dean T Mook. *Nonlinear oscillations*. John Wiley & Sons, 2008.

[5] K. Pyragas. Continuous control of chaos by self-controlling feedback. *Physics Letters A*, 170(6):421–428, 1992.

[6] Jan Sieber, A. Gonzalez-Buelga, S. A. Neild, D J Wagg, and Bernd Krauskopf. Experimental continuation of periodic orbits through a fold. *Physical Review Letters*, 100(24):244101, 2008.

[7] Jan Sieber and Bernd Krauskopf. Control based bifurcation analysis for experiments. *Nonlinear Dynamics*, 51:356–377, 2008.

[8] David A.W. Barton and Stephen G. Burrow. Numerical continuation in a physical experiment: Investigation of a nonlinear energy harvester. *Journal of Computational and Nonlinear Dynamics*, 6(1):011010, 2011.

[9] Emil Bureau, Frank Schilder, Ilmar Santos, Jon Juel Thomsen, and Jens Starke. Experimental bifurcation analysis for a driven nonlinear flexible pendulum using control-based continuation. In *7th European Nonlinear Dynamics Conference*, 2011.

[10] Emil Bureau, Frank Schilder, Ilmar Ferreira Santos, Jon Juel Thomsen, and Jens Starke. Experimental bifurcation analysis of an impact oscillator - Tuning a non-invasive control scheme. *Journal of Sound and Vibration*, 332(22):5883–5897, 2013.

[11] David A.W. Barton and Jan Sieber. Systematic experimental exploration of bifurcations with noninvasive control. *Physical Review E*, 87:052916, 2013.

[12] Ludovic Renson, A. Gonzalez-Buelga, David A.W. Barton, and S. A. Neild. Robust identification of backbone curves using control-based continuation. *Journal of Sound and Vibration*, 367:145–158, 2016.

[13] Ludovic Renson, A. D. Shaw, David A.W. Barton, and S. A. Neild. Application of control-based continuation to a nonlinear structure with harmonically coupled modes. *Mechanical Systems and Signal Processing*, 120:449–464, 2019.

[14] Gleb Kleyman, Martin Paehr, and Sebastian Tatzko. Application of control-based-continuation for characterization of dynamic systems with stiffness and friction nonlinearities. *Mechanics Research Communications*, 106:103520, 2020.

[15] Brandon Gomes, Irene de Cesare, Agostino Guarino, Mario di Bernardo, Ludovic Renson, and Lucia Marucci. Exploring the dynamics of nonlinear biochemical systems using control-based continuation. *bioRxiv*, page 695866, 2019.

[16] David A.W. Barton. Control-based continuation: Bifurcation and stability analysis for physical experiments. *Mechanical Systems and Signal Processing*, 84(B):54–64, 2017.

[17] Ludovic Renson, David A.W. Barton, and S. A. Neild. Experimental tracking of limit-point bifurcations and backbone curves using control-based continuation. *International Journal of Bifurcation and Chaos*, 27(1):1730002, 2017.

[18] L. Renson, J. Sieber, David A.W. Barton, A. D. Shaw, and S. A. Neild. Numerical continuation in nonlinear experiments using local Gaussian process regression. *Nonlinear Dynamics*, 98:2811–2826, 2019.

[19] I. J. Sokolov and V. I. Babitsky. Phase control of self-sustained vibration. *Journal of Sound and Vibration*, 248(4):725–744, 2001.

[20] Sebastian Mojrzisch and Jens Twiefel. Phase-controlled frequency response measurement of a piezoelectric ring at high vibration amplitude. *Archive of Applied Mechanics*, 86(10):1763–1769, 2016.

[21] Simon Peter, Maren Scheel, Malte Krack, and Remco I. Leine. Synthesis of nonlinear frequency responses with experimentally extracted nonlinear modes. *Mechanical Systems and Signal Processing*, 101:498–515, 2018.

[22] Simon Peter and Remco I. Leine. Excitation power quantities in phase resonance testing of nonlinear systems with phase-locked-loop excitation. *Mechanical Systems and Signal Processing*, 96:139–158, 2017.

[23] V. Denis, M. Jossic, C. Giraud-Audine, B. Chomette, A. Renault, and O. Thomas. Identification of nonlinear modes using phase-locked-loop experimental continuation and normal form. *Mechanical Systems and Signal Processing*, 106:430–452, 2018.

[24] Maren Scheel, Simon Peter, Remco I. Leine, and Malte Krack. A phase resonance approach for modal testing of structures with nonlinear dissipation. *Journal of Sound and Vibration*, 435:56–73, 2018.

[25] Maren Scheel, Tobias Weigele, and Malte Krack. Challenging an experimental nonlinear modal analysis method with a new strongly friction-damped structure. *Journal of Sound and Vibration*, 485, 2020.

[26] Taylan Karaağaçlı and H. Nevzat Özgüven. Experimental Identification of Backbone Curves of Strongly Nonlinear Systems by Using Response-Controlled Stepped-Sine Testing (RCT). *Vibration*, 3(3):266–280, 2020.

[27] Taylan Karaağaçlı and H. Nevzat Özgüven. Experimental modal analysis of nonlinear systems by using response-controlled stepped-sine testing. *Mechanical Systems and Signal Processing*, 146, 2021.

[28] Bernard Widrow, Charles S. Williams, John R. Glover, John M. McCool, Robert H. Hearn, James R. Zeidler, John Kaunitz, Eugene Dong, and Robert C. Goodlin. Adaptive Noise Cancelling: Principles and Applications. *Proceedings of the IEEE*, 63(12):1692–1716, 1975.

[29] Simon Haykin. *Adaptive filter theory*. Prentice Hall, New Jersey, 3rd edition, 1996.

[30] Patrick Guillaume, Peter Verboven, Steve Vanlanduit, Herman Van Der Auweraer, and Bart Peeters. A poly-reference implementation of the least-squares complex frequency-domain estimator. *Proceedings of IMAC*, 21:183–192, 2003.

[31] Gaëtan Kerschen, M. Peeters, Jean-Claude Golinval, and Alexander F Vakakis. Nonlinear normal modes, Part I: A useful framework for the structural dynamicist. *Mechanical Systems and Signal Processing*, 23(1):170–194, 2009.

[32] Yang Li and Harry Dankowicz. Adaptive control designs for control-based continuation in a class of uncertain discrete-time dynamical systems. *JVC/Journal of Vibration and Control*, 0(February):1–18, 2020.

[33] G Matheron. Principles of geostatistics. *Economic Geology*, 58:1246–1266, 1963.

[34] Thibaut Detroux, Ludovic Renson, L. Masset, and Gaëtan Kerschen. The harmonic balance method for bifurcation analysis of nonlinear mechanical systems. *Conference Proceedings of the Society for Experimental Mechanics Series*, 1:65–82, 2016.